

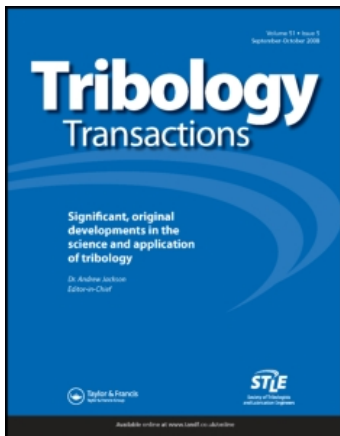
This article was downloaded by: [Arakere, Nagaraj K.][University of Florida]

On: 30 November 2009

Access details: Access Details: [subscription number 906957268]

Publisher Taylor & Francis

Informa Ltd Registered in England and Wales Registered Number: 1072954 Registered office: Mortimer House, 37-41 Mortimer Street, London W1T 3JH, UK



Tribology Transactions

Publication details, including instructions for authors and subscription information:

<http://www.informaworld.com/smpp/title~content=t713669620>

Rolling Contact Fatigue Life and Spall Propagation of AISI M50, M50NiL, and AISI 52100, Part II: Stress Modeling

Nagaraj K. Arakere ^a; Nathan Branch ^a; George Levesque ^a; Vaughn Svendsen ^b; Nelson H. Forster ^b

^a Mechanical & Aerospace Engineering, University of Florida, Gainesville, Florida, USA ^b Air Force Research Laboratory, Wright-Patterson Air Force Base, Ohio, USA

First published on: 30 November 2009

To cite this Article Arakere, Nagaraj K., Branch, Nathan, Levesque, George, Svendsen, Vaughn and Forster, Nelson H.(2009) 'Rolling Contact Fatigue Life and Spall Propagation of AISI M50, M50NiL, and AISI 52100, Part II: Stress Modeling', Tribology Transactions, 53: 1, 42 – 51, First published on: 30 November 2009 (iFirst)

To link to this Article: DOI: 10.1080/10402000903226325

URL: <http://dx.doi.org/10.1080/10402000903226325>

PLEASE SCROLL DOWN FOR ARTICLE

Full terms and conditions of use: <http://www.informaworld.com/terms-and-conditions-of-access.pdf>

This article may be used for research, teaching and private study purposes. Any substantial or systematic reproduction, re-distribution, re-selling, loan or sub-licensing, systematic supply or distribution in any form to anyone is expressly forbidden.

The publisher does not give any warranty express or implied or make any representation that the contents will be complete or accurate or up to date. The accuracy of any instructions, formulae and drug doses should be independently verified with primary sources. The publisher shall not be liable for any loss, actions, claims, proceedings, demand or costs or damages whatsoever or howsoever caused arising directly or indirectly in connection with or arising out of the use of this material.

Rolling Contact Fatigue Life and Spall Propagation of AISI M50, M50NiL, and AISI 52100, Part II: Stress Modeling

NAGARAJ K. ARAKERE¹, NATHAN BRANCH¹, GEORGE LEVESQUE¹, VAUGHN SVENDSEN²,
and NELSON H. FORSTER²

¹Mechanical & Aerospace Engineering
University of Florida, Gainesville
Florida 32611-6300, USA

²Propulsion Directorate
Air Force Research Laboratory
Wright-Patterson Air Force Base, Ohio 45433, USA

This is the second part of a three-part series that investigates the rolling contact fatigue initiation and spall propagation characteristics of three bearing materials, namely, AISI 52100, VIM-VAR M50, and VIM-VAR M50NiL steels. A systematic investigation of the effects of rolling contact fatigue (RCF) on the evolution of material properties and microstructural changes resulting in spall propagation rate has not been conducted. As a first step toward understanding spall propagation, we present stress distribution in the neighborhood of a spall initiated by RCF by an indent on a hybrid 40-mm ball bearing. Elastic and elastic-plastic subsurface stress fields are computed using finite element models that incorporate the full three-dimensional (3D) ball-raceway geometry. The stress fields predicted indicate extensive yielding around the spall edges. The spall is shown to widen first axially across the width of the raceway, causing the ball to unload as it enters the spall. The effect of the potential impact on the spall trailing edge is also considered. The proposed scenario involves repeated application of contact stress resulting from a combination of ball static and the impact loads results in extensive plastic deformation of the spall trailing edge, leading to degradation and release of material resulting in spall propagation.

KEY WORDS

Spall Propagation; Ball Bearings; Contact Mechanics; Fatigue Analysis; Bearing Steels; Gas/Jet Engines; Impact Wear; Rolling-Contact Fatigue; Elastic-Plastic Stress Analysis; Finite Element Analysis

INTRODUCTION

Aircraft engine and bearing manufacturers have been aggressively pursuing advanced materials technology systems solutions to meet the main shaft-bearing needs of advanced military en-

gines. Such efforts are aligned with goals for affordable high speed, high life bearings that have superior durability, and corrosion resistance. Desirable near- and long-term attributes of an advanced main-shaft bearing to meet the challenging requirements of future advanced military engines include rolling contact fatigue life greater than five times M50 steel, core fracture toughness greater than M50-NiL, corrosion resistance greater than AISI 440C, tribological performance greater than M50 steel (increased oil out capability, lower heat generation, and performance under boundary lubrication conditions), and affordable life cycle cost. These requirements have led to the development of hybrid bearings with silicon nitride balls and metal raceways made of materials such as case-hardened Pyrowear 675 (P675) and M50NiL and through-hardened M50. The rolling contact fatigue (RCF) performance of hybrid ceramic/steel bearings has been shown to be much superior to steel bearings (Miner, et al. (1); Tanimoto, et al. (2); Wang, et al. (3); Hadfield (4); Hadfield and Stolarski (5)).

Past bearing material programs typically used life as the primary measure of performance; i.e., the time until initiation of the failure. However, there is also a desire to understand what happens after initiation; i.e., the period of time where the bearing is liberating small pieces of material known as spalls. It is this window where bearing issues in the field are detected, usually from the spalled material collected on the magnetic chip detector. The objective of the research described in this Part II article is to model the elastic-plastic stress field associated with the loaded region undergoing spall propagation. In Part I, Rosado and Forster (6) showed that M50 and M50 NiL bearings had much longer fatigue life and longer propagation times to reach the same level of damage under the same Hertzian contact stress as the 52100 bearings. The Part III article by Forster, et al. (7) investigates three bearing steels (AISI 52100, VIM-VAR M50, and VIM-VAR M50 NiL) with distinct microstructures to examine the effects of alloy content, heat treatment, and applied stress field on the rolling contact fatigue initiation and spall propagation characteristics. This three-part series of articles represents the first attempt at a systematic investigation of spall propagation and may provide engineers guidance to decrease the spall propagation rate, thereby improving the safety of bearings in the field.

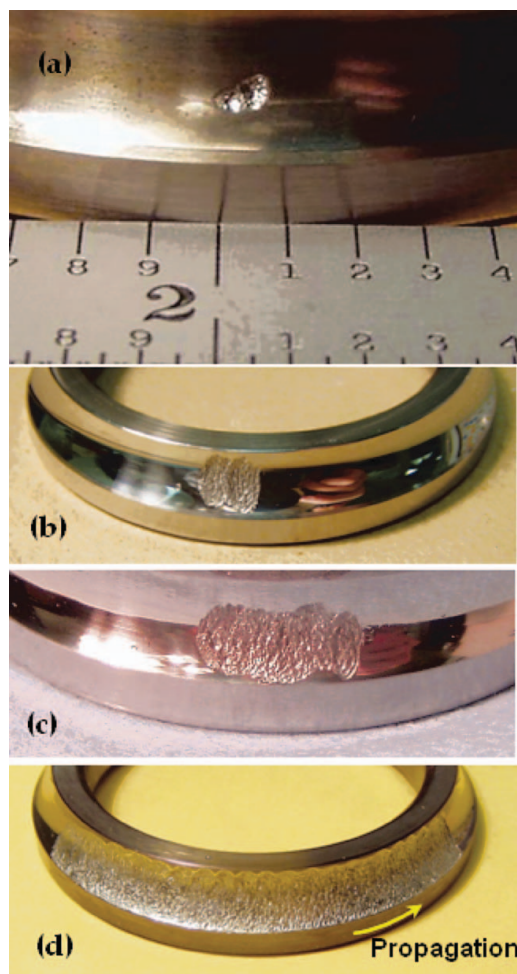


Fig. 1—Fatigue spall initiation on inner raceway; (b), (c), and (d) show progressive propagation of the initiated spall under continued RCF.

Figure 1 shows an initiated fatigue spall and its progressive propagation under RCF in a M50 ball bearing raceway. Data suggest that material properties, microstructure, residual compressive stress, and the selection of oil additives affect the rate of failure, but there has never been a bearing program to specifically address the material and lubrication technologies for extending the time from initiation until catastrophic failure occurs. Recent studies at the Air Force Research Labs (AFRL), Dayton, OH (Rosado and Forster (6); Forster, et al. (7)), of the next generation bearing race materials indicate that both qualitative and quantitative observations of the spall propagation performance warrant further investigation into the fundamental mechanisms that control this behavior as well as an attempt to model the propagation behavior itself. The observations under this program ranged from spalls that propagated in a more controlled manner characterized by smaller particles and flakes being generated and departing from the race, as typically observed in rolling contact fatigue, to spalls that were characterized by large pieces or even chunks being generated as the spall lengthened. Under some test conditions, the propagation rate of the spall reaches a point at which these large pieces depart from the raceway very rapidly.

The latter observations were in a race material that in all other aspects had performed extremely well; i.e., exhibited a resistance to surface damage initiation as well as tolerance of such damage and thus had an extended fatigue life. Figure 2 summarizes aspects of the complex interplay between the maximum Hertz stress, material selection, and the spall propagation rate, as measured by the bearing mass loss (Rosado and Forster (6)). Tests were conducted at the same temperature for both 52100 and M50 NiL materials. We note that 52100 steel shows rapid spall propagation at 1.917 GPa (278-ksi) max Hertz stress. Even at 1.724 GPa (250-ksi) peak Hertz stress the propagation rate is significant and if increased to 1.917 GPa (278 ksi) during operation the rate increases very quickly. In contrast, M50NiL generally did not propagate a spall at 2.069 GPa (300 ksi) and in instances when it did it took considerably longer than for 52100. At this lower stress level greater variance in the time for spall propagation was observed with M50NiL and M50. If the stress level is increased to 2.41 GPa (350 ksi) the increase in the spall propagation rate is more gradual than for the 52100 material. Clearly there are interactions between the stress level and as yet unknown material parameters that affect the spall propagation rate that are not understood.

BACKGROUND

The goals of this article are to understand the damage mechanisms that lead to propagation of an initiated fatigue spall, as depicted in Fig. 1, and parameters that control the rate of propagation (Fig. 2). However, it is beneficial to first examine the current state of understanding of damage evolution that leads to fatigue spall initiation. The cyclic plastic strains generated by RCF in ball bearings, beyond the shakedown limit, are typically $0 \leq \Delta \epsilon^{pl} \leq 0.003$, and depend on the cyclic yield strength and the character of the cyclic stress-strain relations (Hahn, et al. (8)). However, the cyclic stress-strain parameters are rarely used to characterize RCF life in rolling element bearings.

In a series of articles since the early 1980s to the present, Voskamp and Osterlund (9); Voskamp (10), (11); Voskamp and Mittemeijer (12); Voskamp (13); Voskamp and Mittemeijer (15); and Voskamp, et al. (14) have described in detail the evolution of material degradation due to RCF in ball bearing inner ring raceways that lead to a spall. Voskamp (10), (11) and Voskamp and Mittemeijer (12) noted that the high level of cleanliness of bearing steels in current bearing technology is not the only decisive factor in minimizing the probability of fatigue spalls. The second very important factor is the microplastic deformation behavior of bearing steel under the action of RCF. The buildup of residual stress provides an indirect measure of microplastic deformation and can be quantified by X-ray diffraction methods (Forster, et al. (7); Voskamp, et al. (14); Voskamp and Mittemeijer (15); Dommarco (16)).

Voskamp and his coresearchers (Vingsbo and Osterland (9); Voskamp (10), (11); Voskamp and Mittemeijer (12); Voskamp (13); Voskamp et al. (14); Voskamp and Mittemeijer (15)) describe the material degradation due to RCF in ball bearing inner rings as a three-stage process, briefly identified as follows: (I) shakedown, (II) steady-state elastic response, and (III) instability. During the shakedown stage a residual stress is induced with an increase in material strengthening and micro-yield

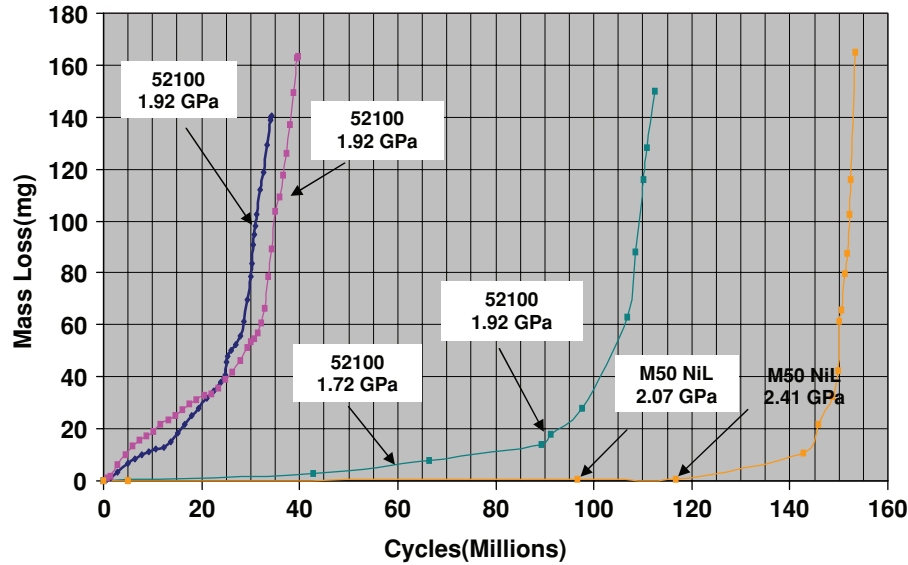


Fig. 2—Effect of maximum inner raceway Hertz stress (ksi) and material selection on the loss of raceway material due to spall propagation (Rosado, et al. (6)). Note that M50 NiL will not propagate a spall at 2.069 GPa (300 ksi), while 52100 has a very rapid spall propagation rate at 1.917 GPa (278 ksi).

stress, due to work hardening and also likely due to the transformation of the part of the retained austenite to the martensite (Voskamp and Mittemeijer (12); Tuttle and Suiker (17)). The sensitivity of bearing fatigue life to slight changes in temperature has been observed in several investigations (Rosado and Forster (6); Forster, et al. (7); Voskamp (10); Voskamp and Mittemeijer (12)). Stage III is marked by a decrease in yield stress due to material softening, causing an increase in subsurface volume that is deformed plastically. The development of a radial tensile stress and texture development promotes growth of cracks parallel to the rolling surface (Voskamp (13); Voskamp and Mittemeijer (18)).

This description of damage evolution leading to a fatigue spall was included to highlight the lack of a similar level of understanding for spall propagation. Kotzalas and Harris (21) have looked at fatigue failure progression of ball bearings in a v-ring test and concluded that excessive vibration was the determining factor in component failure. Xu and Sadeghi (22) developed an analytical model to investigate the effects of dent on spall initiation and propagation. Understanding the effects of the stress level on the evolution of cyclic bearing material parameters and their effect on the spall propagation rate is important. This will entail the development of a comprehensive 3D elastic-plastic finite element model with known cyclic constitutive parameters for bearing steels. As a first step towards understanding spall propagation, a simplified analysis of the 3D elastic-plastic static stress field in the neighborhood of a circular spall on the inner raceway as a ball rolls over the spall is presented. Based on the nature of yielding on the spall edge due to rolling contact, a scenario is proposed that is quite effective in explaining certain qualitative aspects of spall propagation observed in testing. This Part II article, along with Parts I and III (Rosado and Forster (6); Forster, et al. (7)), represents the first attempt to systematically study spall propagation behavior in ball bearings.

Spall Propagation Characteristics

The test bearing is a split-inner ring 40-mm hybrid with M50 NiL raceways and 12.7-mm (0.5-in.)-diameter silicon nitride balls. The description of the test rig and testing procedures is described in Part I of this three-part series of articles (Rosado and Forster (6)) and the metallurgical examination of the raceways is presented in Part III (Rosado and Forster (6)). Figure 3(a) shows a schematic of a spall on the inner raceway along with bearing kinematics details. For an inner ring speed of 10,000 RPM, cage RPM is 4,023 and ball RPM is 22,814. The inner raceway speed relative to the ball is 15.18 m/s (49.8 ft/s). We now revisit the spall propagation illustrated in Fig. 1. Figure 1(a) shows the as-initiated spall on the inner ring raceway. The peak Hertz raceway stress during testing is 2.41 GPa (350 ksi). Figure 1(b) shows the typical progression of the spall under continued RCF. The spall first widens almost across the entire width of the raceway. The depth of the spall is roughly 125 μm (0.005 in.). Once the spall spans the axial width of the raceway propagation it is seen to proceed in the direction away from the initial spall leading edge, in the circumferential direction. Based on testing, modeling, and metallurgical investigation (Rosado and Forster (6), (7)) a three-step process is outlined below to explain the progressive damage evolution caused by spall propagation:

1. Material on the edges of the spall yields due to RCF. The yield stresses induced by the ball rolling on the spall are higher on the diametral edges of the spall along the shaft axis than at the spall leading and trailing edges. This scenario will be substantiated with 3D FEA modeling of the stresses in the neighborhood of the spall due to rolling and via hardness measurements near the spall (Rosado and Forster (7)). Material degradation from repeated rolling causes the spall to widen as shown in Fig. 1(b). The spall width eventually spans the width of the raceway, as seen in Fig. 1(c).

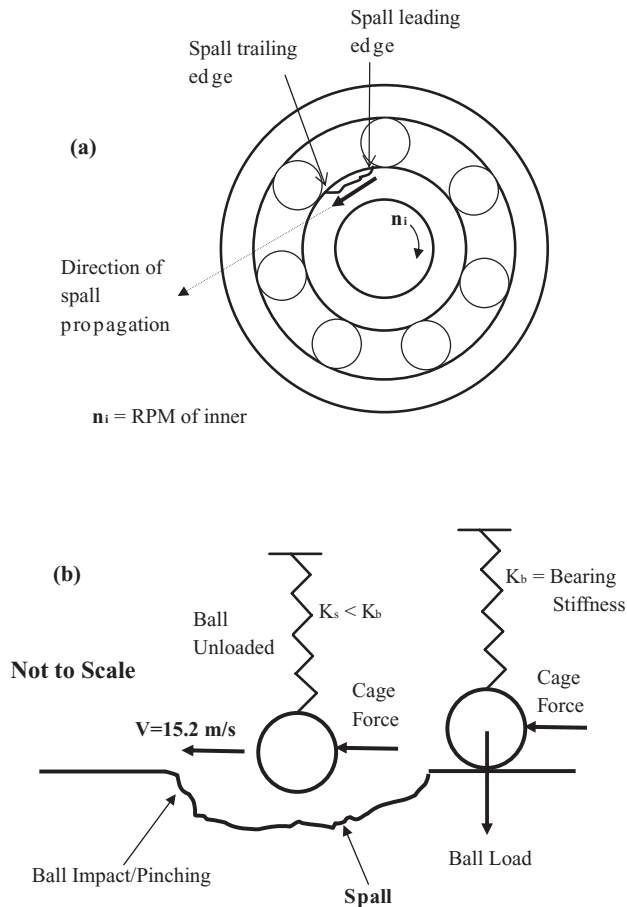


Fig. 3—(a) Test bearing schematic showing the inner ring spall as a blue line. For $n_i = 10,000$ RPM, cage RPM is 4,023 and ball RPM is 22,814. Inner raceway speed relative to the ball is 15.18 m/s (49.8 ft/s). **(b)** Schematic explaining the unloading of the ball in the spall and subsequent impact resulting in yielding at the spall trailing edge.

2. Widening of the spall allows for the ball to descend into the spall. Since the spall depth ($125 \mu\text{m}$, 0.005 in.) is greater than the bearing radial internal clearance the ball will unload, illustrated in Fig. 3(b). The load supported by this ball is then shared by other loaded balls in the bearing, leading to a change in the effective bearing stiffness.
3. As the ball moves through the spall length, pushed along by cage interaction forces, it will partially impact the spall trailing edge as it climbs onto the intact raceway (Fig. 3(b)). The stresses arising from the impact along with the contact stresses results in severe fatigue of the spall trailing edge material, leading to the propagation of the spall in the direction indicated in Fig. 1(d) and Fig. 3(a). Estimation of impact stresses at the trailing edge will be explained in a later section.

Analytical Procedure

A 3D finite element (FE) model was built using ABAQUS 6.7 (19) to model the stress state as a silicon nitride ball goes over a circular raceway spall in a bearing application. The FE model is an accurate representation of the full 3D ball–inner raceway con-

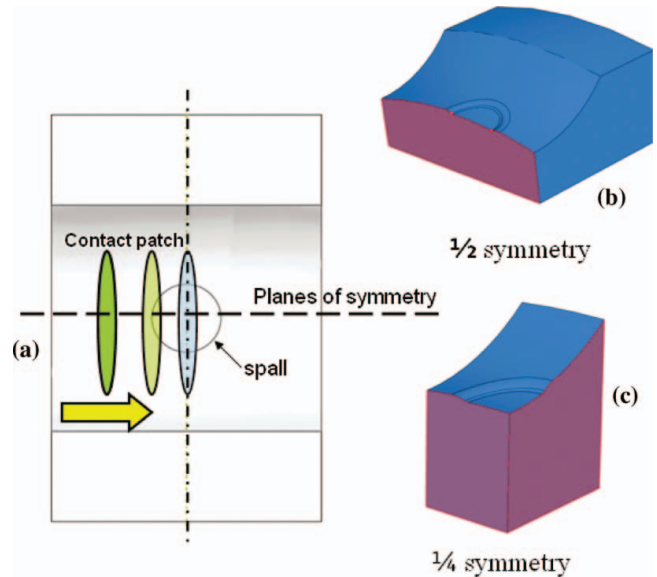


Fig. 4—(a) Illustration of contact patch's position as the ball goes over the raceway's spall. Also displays the planes of symmetry used to create models: **(b)** $1/2$ symmetry and **(c)** $1/4$ symmetry.

tact geometry, as shown in Figs. 4 and 6. The test bearing material and geometric properties are shown in Table 1. The FE model created here is similar to that by Zaretsky, et al. (20). Mesh refinement tests were performed for both tetrahedral and hexahedral elements such that the converged results for the Hertz peak elliptical contact stress agreed to within 1% of the analytical solution. Tetrahedral linear elements were used because of their ability to easily mesh complex geometries, such as the edge of a spall. The severe stress concentrations imposed by the elliptical contact and spall geometry required very refined contact mesh geometry for obtaining acceptable solutions. Also, the use of linear tetrahedral elements proved to be more efficient than quadratic elements, based on achieving a balance between the solution accuracy and run time.

Half-symmetry modeling was used since the contact patch load and the bearing geometry were symmetric. Quarter symmetry was used for the unique case when the ball is directly over the center of the spall. Figure 6 illustrates this. The stress concentration created by the spall edge radius was found to greatly influence the severity of the stress state, as illustrated in Fig. 7. The spall edge radius was chosen to be 1 mm, based

TABLE 1—TEST BEARING MATERIAL AND GEOMETRIC PROPERTIES

E = Elastic modulus, ν = Poisson's ratio	
Steel raceway	E = 200 GPa, $\nu = 0.3$
Silicon nitride	E = 310 GPa, $\nu = 0.3$
Raceway yield stress, Y = 2.34 GPa (340 ksi) silicon nitride ball diameter	12.7 mm
Inner raceway curvature, f_i	0.52
Inner ring bore	40 mm
Bearing pitch diameter	60.24 mm
Inner raceway radius	23.77 mm

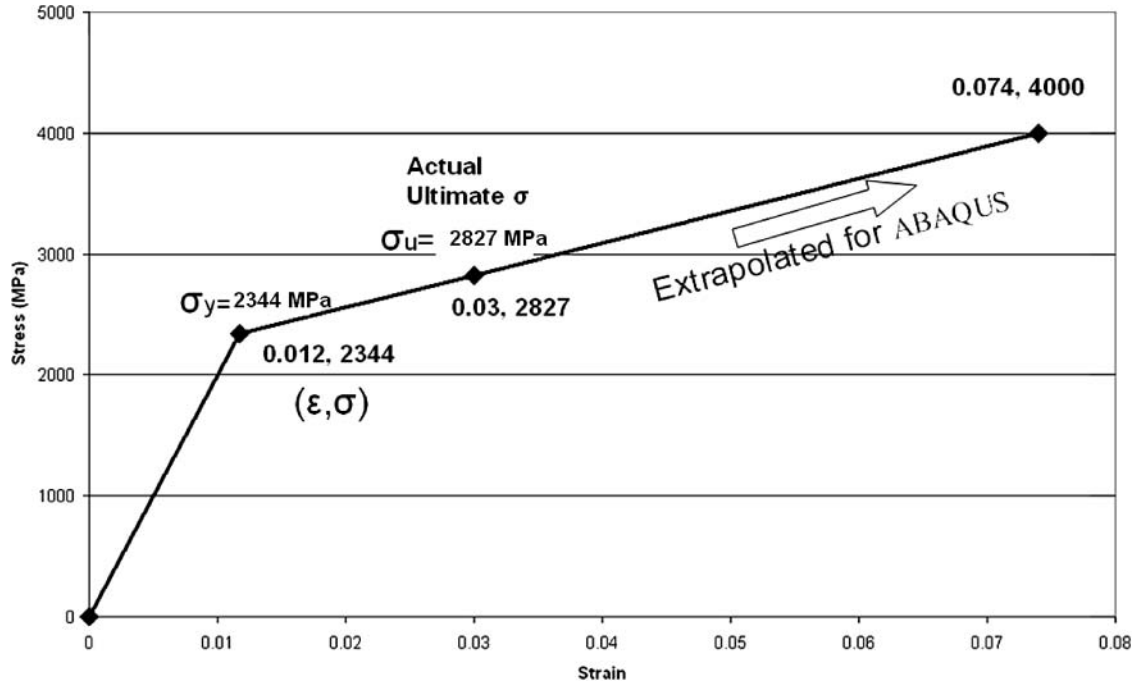


Fig. 5—Linear elastic and plastic strain hardening material properties input to ABAQUS for raceway steel. The stress strain curve is extrapolated past the ultimate strength in order to allow ABAQUS to converge to a value. The plastic modulus remains constant past this point.

on meshing and convergence considerations. The depth of the spall was chosen to be $125\ \mu\text{m}$ ($0.005\ \text{in.}$), based on experimental measurements. The spall diameter is used as a parameter in the analysis. The normal load applied to the ball to achieve a peak Hertz contact stress of $2.65\ \text{Mpa}$ ($385\ \text{ksi}$) on the inner raceway is $1630\ \text{N}$ ($366\ \text{lb}$).

Finite element simulation of the loaded ball, with a peak Hertz contact stress of $2.65\ \text{Mpa}$ ($385\ \text{ksi}$) away from the spall, rolling over the spall is accomplished via a series of single static load cases. The spall diameter is treated as a variable. Dynamic loading effects such as yield strength dependency on the applied strain

rate are not included. Also, initial residual stresses from case or work hardening were not included. These aspects as well as the unloading effects are not studied here but will be considered in forthcoming studies.

Linear elastic analysis of the stress field in the neighborhood of the spall, caused by ball rolling, indicated that stresses everywhere on the edge of the spall exceeded the ultimate tensile strength. This is not surprising since both nonconformal contact loading and the spall surface geometry represent severe stress concentrations. For a more realistic stress field computation we used elastic-plastic FEA. The use of the associated flow rule to calculate increments of plastic deformation, as implemented in ABAQUS (19), was utilized for modeling the elastic-plastic behavior. Linear isotropic hardening was used in the models that included the plastic regime of the material's stress-strain curve, shown in Fig. 5. This is a valid assumption since isotropic, kinematic, and combined isotropic and kinematic hardening laws all

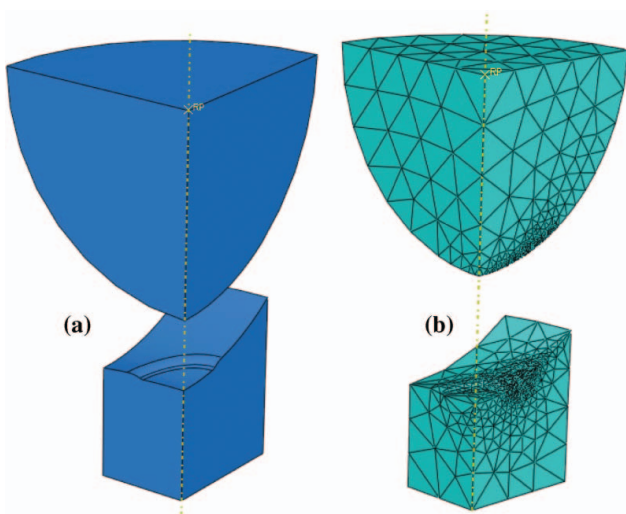


Fig. 6—Three-dimensional FEA model using quarter symmetry when the ball is positioned over the center of the spall; (a) model geometry, (b) meshed FEA model.

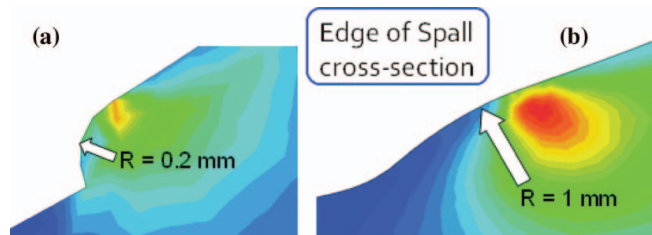


Fig. 7—Cross section of the edge of spall. The radius of curvature of the edge of the spall affects the severity of the stress state. (a) “Sharp” edge of spall, max elastic von Mises stress = $8\ \text{GPa}$ compared to converged value of (b) $4\ \text{GPa}$ for “rounded” spall edge.

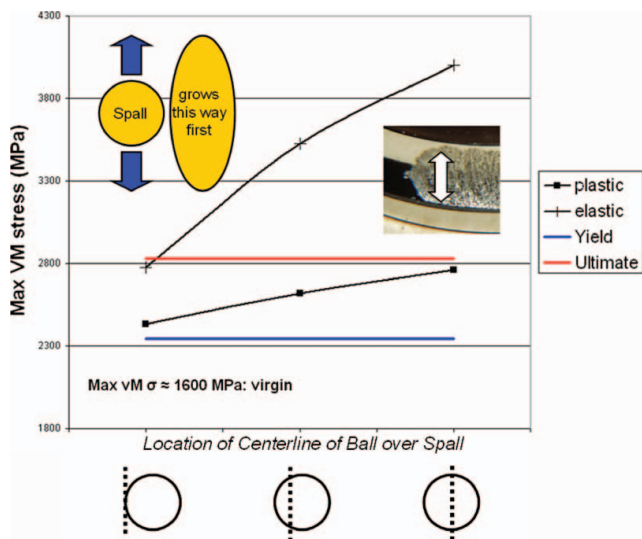


Fig. 8—Plot of maximum subsurface von Mises stress as a function of the ball's 3 mm * 0.4 mm contact patch position over the 3-mm circular spall. Stresses are the highest when the ball is directly over the center of the circular spall. Load applied to the ball is the same load that results in a 2.65 GPa (385 ksi) max contact pressure seen by the virgin raceway.

converge to the same stress solution for static monotonic loading. It is during unloading and subsequent load cycles that these laws begin to display different behavior. For example, the combined isotropic and kinematic hardening rule can be used to simulate the evolution of shakedown and ratcheting. The effects of cyclic hardening rules on spall propagation will be explored in subsequent studies.

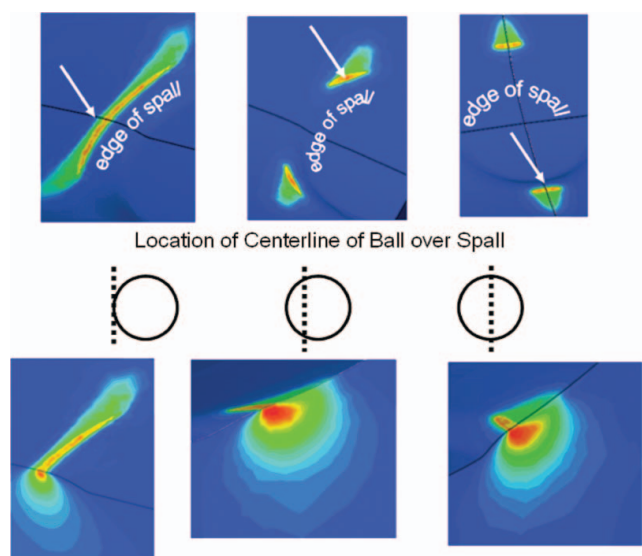


Fig. 9—Plot of von Mises stress state for three different positions of the ball over the spall: (a) edge, 2.433 GPa (b) 1/4th into the spall, 2.617 GPa (c) center, 2.763 GPa. Note that stress magnitude is highest at the axial diametral locations of spall for (c). White arrows show the location of maximum von Mises stress.

RESULTS AND DISCUSSION

Three-dimensional linear-elastic and elastic-plastic finite element modeling results of the spall edge stresses due to rolling contact are discussed first. The spall trailing edge stresses due to ball impact, based on a simplified analytical approach and an explicit finite element approach, are presented next.

Spall Edge Stresses from Rolling Contact

Figure 4a shows a schematic of the ball elliptical contact patch moving over the circular spall. Figure 8 depicts the maximum subsurface von Mises stress in the neighborhood of the spall edge as a ball rolls over a 3-mm-diameter circular spall, as indicated in Fig. 4a. The peak Hertz contact stress away from the spall is 2.65 Mpa (385 ksi), as indicated earlier. The results are shown for three different positions of the ball over the spall—at the leading edge, between the edge and the center, and directly over the center. The blue line represents the static yield strength limit, and the red line represents the static ultimate strength limit. The elastic stresses exceed the yield and even the ultimate strength for all positions of ball with respect to the spall. The von Mises stresses are highest when the ball is in the center of the spall and the lowest when it is at the edge. It is important to note that the magnitude of von Mises stress is highest on the axial diametral locations, indicating that the spall widens due to RCF in the axial direction spanning the width of the raceway, as shown in Fig. 1(b), before propagating along the raceway in the circumferential direction, as shown in Figs. 1(c) and 1(d). On reflection, this is intuitive since there is less material supporting the ball when it is in the center of the spall than when it is on the spall's edge. Figure 9 displays cross sections of the von Mises stress contours for the three “ball-over-spall” positions. Figure 10 shows the effect of increase in the peak Hertz stress on spall edge stresses for on-center loading. It also shows that the volume of the yielded material around the spall increases with increasing operating load. This also helps to confirm that the material removal rate is higher for increasing operating loads since the damage accumulation is faster due to the higher stresses within the spall. We note that the peak plastic stress has exceeded the ultimate tensile strength. This is a consequence of the linear extrapolation used in the stress-strain curve with a constant plastic modulus, as shown in Fig. 5. A suitable nonlinear fit for the stress-strain curve will resolve this concern. Figure 11 shows a closeup of the von Mises stress contours at the edge of a spall. The high stress gradients indicate that they are potential sites for damage initiation. Figure 12 demonstrates that the maximum von Mises stress experienced in the spall edge region increases with spall diameter for both elastic and plastic analyses.

Impact Stress at the Spall Trailing Edge: Analytical Approach

In the spall propagation characteristics section it was proposed that the spall widens first in the axial direction (Fig. 1(b)), spanning the width of the raceway and, eventually, allowing the ball to descend into the spall causing the ball to unload (Fig. 3(b)). When the spall becomes large enough for a single ball to unload, the ball is free to move through the cage-ball clearance. During impact, a

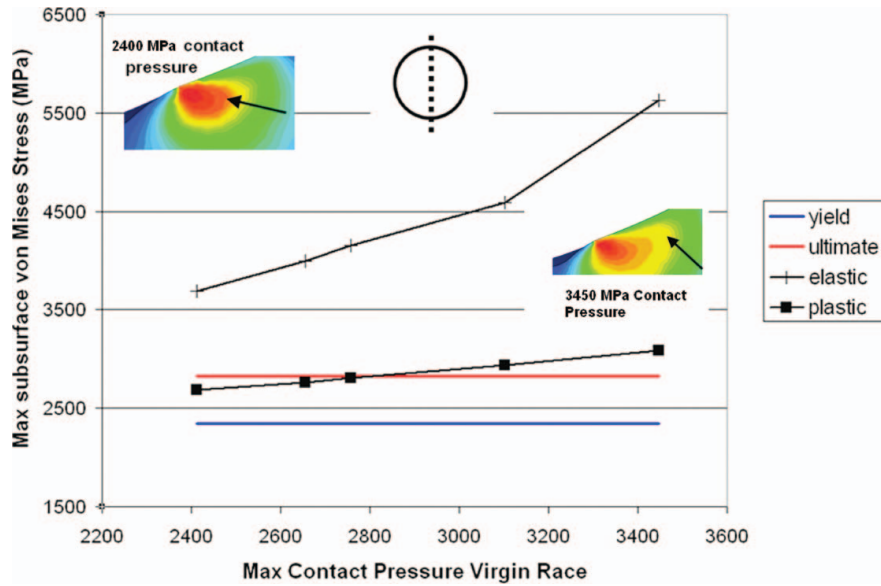


Fig. 10—Graph of maximum subsurface stress located at the edge of the spall as the load on the ball is increased through the range of maximum contact stress seen on the virgin raceway. Black arrows indicate zone of yielded material. Blue line indicates the yield stress limit and the red line the ultimate stress limit.

portion of the cage mass likely contributes to the effective impact mass. As the spall propagates long enough for two or more balls to be unloaded in the spall, estimating the effective impact mass gets more complicated. Since this is a first investigation of spall propagation, the effective impact mass is assumed to be that of the ball alone. Under the test bearing conditions, this unloaded ball is moving at 15.2 m/s relative to the inner raceway. As the ball approaches the trailing edge, the lower portion of the ball will impact or partially impact (pinch) the oblique edge. Once the ball climbs onto the raceway it is loaded and will establish the Hertz contact stress, as computed in the FE model. Hence, the trailing edge of the spall is likely to experience stress from the ball impact loading while the trailing edge surface on the raceway will experience the Hertz contact stress. The repeated application of this combined loading due to RCF is thought to weaken the inside spall edge material, leading to spall propagation along the raceway circumference, as shown in Figs. 1(d) and 3(a). A detailed analysis of a silicon nitride ball impacting an oblique surface, accounting for the proper raceway and cage constraints, is

expectedly very complicated. In reality, the dynamics of ball interaction with the spall will affect the motions of the inner ring, the outer ring, the cage, the ball unloading, and the potential energy in the loaded contacts opposite of the spall in complex ways. This complex coupled system interaction will most likely result in higher dynamic loads. Such interactions can only be adequately modeled in a coupled three-dimensional rolling-element bearing dynamics simulation (Gupta (23)). However, the assumptions in this modeling do allow an exploration of the stresses and differences in materials. A lower bound estimate can be obtained by performing a simplified impact analysis of a rigid 12.7-mm (0.5 in.)-diameter ball with a density of 2,600 kg/m³ for silicon

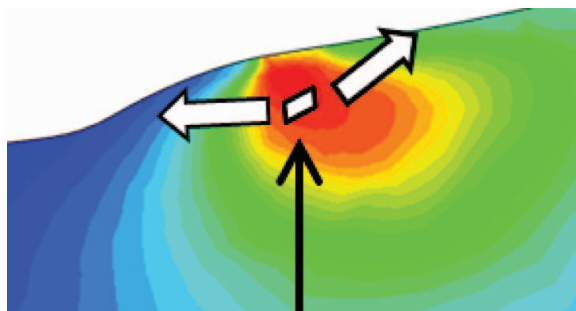


Fig. 11—Closeup of a typical von Mises stress contour at the spall edge. The plastic zone is indicated by the red zone. The tensile hydrostatic stress and steep von Mises stress gradients indicate this is a possible damage initiation site.

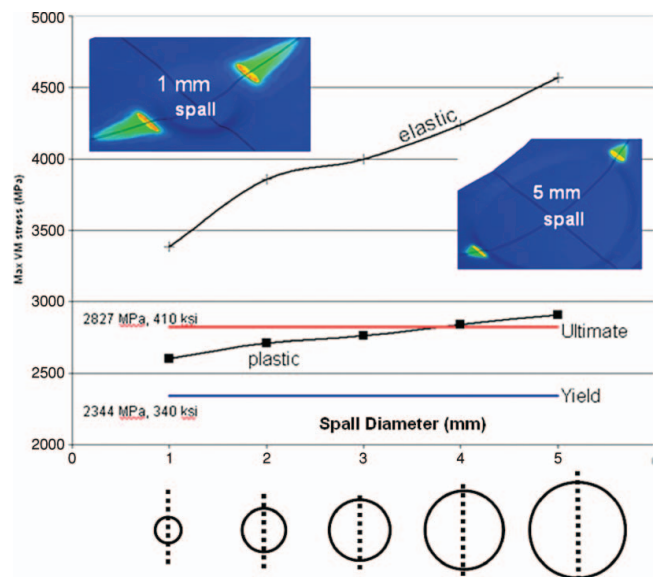


Fig. 12—Plot of maximum subsurface von Mises stress as a function of spall diameter.

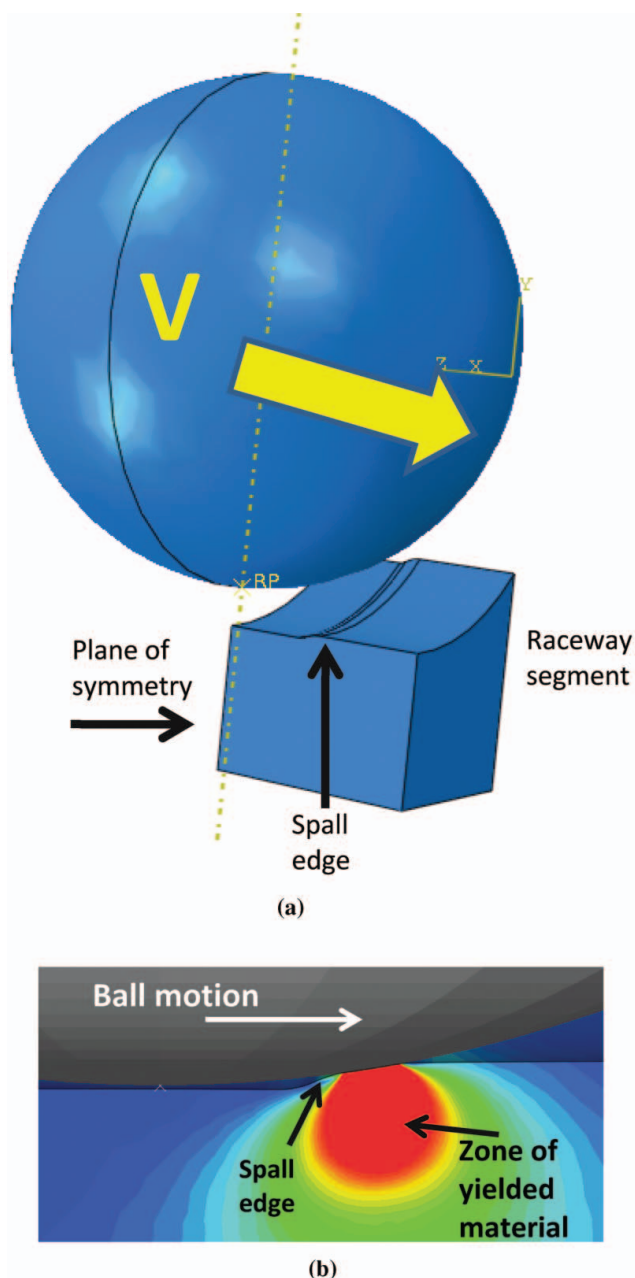


Fig. 13—Analysis of ball impact with spall edge using ABAQUS Explicit: (a) Solid model of the ball and raceway segment with the spall edge. Ball velocity, $V = 15.2$ m/s (50 ft/s). (b) Closeup view of the spall edge showing the zone of yielded material resulting from the ball impact.

nitride, striking a ductile metallic oblique surface at a 45-degree angle to horizontal, based on Johnson (24), using equation shown below

$$P_o = \frac{3}{2\pi} \left(\frac{4E^*}{3R^{3/4}} \right)^{4/5} \left(\frac{5}{4} mV^2 \right)^{1/5} \quad [1]$$

For an impact velocity of $V = 15.2$ m/s (50 ft/s), the estimated peak contact stress, p_o , at the spall trailing edge during impact is ~ 5.2 GPa (750 ksi), using Eq. [1]. Subsurface yielding is predicted if the maximum contact pressure reaches $1.6 * Y$ where Y is the

material yield stress (Gupta (23)). Using a yield stress of 2.34 GPa (340 ksi) and accounting for an increased value for the dynamic yield stress (Johnson (24); Rickerby and McMillan (25)), yielding is predicted at the spall trailing edge for a peak contact pressure above 4.9 GPa (710 ksi). Rickerby and McMillan (25) and Hutchings, et al. (26) have conducted investigations of oblique impact of a 9.5-mm-diameter hard sphere against a ductile solid for a range of moderate impact velocities and angles. Based on their measurements of impact damage, the loss of kinetic energy, induced stress, crater volume, and modeling results, the yielding prediction under impact presented here is likely conservative. Thus, the combined effects of repeated applications of impact and contact stress at the spall trailing edge are thought to initiate material degradation and eventually spall propagation along the raceway, as shown in Fig. 1.

Impact Stress at the Spall Trailing Edge: Explicit Finite Element Approach

For a better estimation of the contact stresses in the vicinity of the spall, the above impact problem was also simulated using ABAQUS Explicit via an elastic-plastic dynamic analysis of a ball striking the edge of a spall as seen in Fig. 13. For this case the ball was assumed to be analytically rigid and the influence of the curvature of the raceway in the circumferential direction was assumed to be negligible. The same material properties used in the static analysis were also used here since the strain rate-dependent material properties are not yet readily available for these bearing steels. The geometry of the spall is the same as in the static analyses. Figure 13b shows a closeup view of the spall edge with the plastically deformed subsurface region shown in red resulting from the impact. The time-transient subsurface stress evolution during the ball impact to the spall edge is captured using an explicit dynamic simulation. The explicit approach necessitates a very small time step of 7.88×10^{10} s for numerical stability. Based on the ball velocity of 15.2 m/s (50 ft/s), the total simulation time elapsed during impact is 3.5×10^5 s, requiring a total of 44,416 explicit time step increments to simulate a single impact of the ball with the spall edge.

Figure 14 shows the evolution of the contact pressure, the maximum von Mises stress, and the maximum principal stress during impact. The important conclusion from Fig. 14 is that yielding occurs within the edge of the spall during impact. This agrees with the simplified analytical solution discussed before. The maximum contact pressure also reaches a high value of 7.8 GPa during contact. The maximum von Mises stress exceeds the ultimate tensile strength of the material within the spall during impact because of the extrapolated material properties used in the elastic-plastic stress-strain curve (Fig. 5), taken from static material tests. Since most materials experience an increase in material strength under dynamic loading, the dynamic ultimate strength defined here was allowed to exceed the static value. The residual stress states in the radial and the hoop direction, after unloading of the ball, are of practical interest for spall propagation analysis and will be the subject of subsequent analyses.

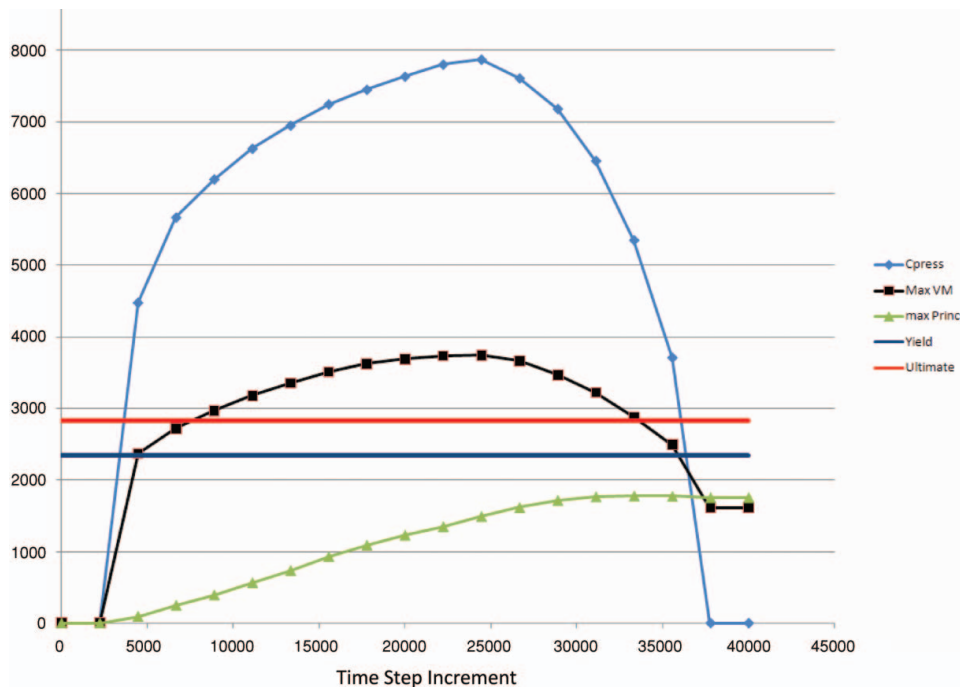


Fig. 14—Evolution of contact pressure, maximum von Mises stress, and maximum principal stress, as a function of time step increment during a single impact. Time step increment, $\Delta t = 7.88 \times 10^{10}$ s. Total simulation time during impact = 3.5×10^5 s.

CONCLUSIONS

Based on results from 3D FE stress analysis in the spall neighborhood, the simplified trailing edge impact stress analysis, the dynamic finite element impact analysis of the ball with the spall edge using ABAQUS Explicit, and the spall propagation tests (Rosado and Forster (6); Forster, et al. (7)) the conclusions are as follows:

1. Elastic and elastic-plastic 3D FEA of the stress field in the neighborhood of a circular spall shows that there is extensive yielding at the spall edges due to ball rolling contact. The stress magnitudes are highest at the axial diametral locations of the spall.
2. It is hypothesized that the spall first widens in the axial direction, spanning the width of the inner raceway (Fig. 1(b)). This allows the ball to descend into the spall, causing it to unload (Fig. 3(b)).
3. The unloaded ball then catches up to the spall trailing edge, resulting in an impact with the oblique edge. The impact stress, estimated via simplified analysis, was shown to be adequate to cause yielding of the trailing edge. A time-transient finite element analysis of the ball impact with the spall edge is performed using ABAQUS Explicit. Computed results of the evolution of the spall edge stresses during impact confirm extensive yielding of the spall edge material as a result of the impact.
4. The combined effects of repeated impact and contact stress at the spall trailing edge results in material degradation, resulting in the propagation of the trailing edge in the circumferential direction (Fig. 1(d)).

Future studies will incorporate the effects of variation in impact mass, repeated ball impact of the spall edge, the effects of cyclic plasticity, plastic shakedown, and the buildup of residual stresses.

ACKNOWLEDGMENTS

This work was supported by the Air Force Research Labs (AFRL), Dayton, OH. The authors, affiliated with the University of Florida, would like to thank ASEE/AFOSR summer faculty and accompanying graduate student fellowship program for their support and for allowing them to complete this work at AFRL during the summer of 2007.

REFERENCES

- (1) Miner, J.R., Dell, J., Galbato, A. and Ragen, M.A. (1996), "F-117-PW-100 Hybrid Bearing Ceramic Technology Insertion," *ASME J. Engineering Gas Turbines Power*, **118**, pp 434-442.
- (2) Tanimoto, K., Kajihara, K. and Yanai, K. (2000), "Hybrid Ceramic Ball Bearings for Turbochargers," *SAE Paper 2000-01-1339*.
- (3) Wang, L., Snidle, R.W. and Gu, L. (2000), "Rolling Contact Silicon Nitride Bearing Technology: A Review of Recent Research," *Wear*, **246**, pp 159-173.
- (4) Hadfield, M. (1998), "Failure of Silicon Nitride Rolling Elements with Ring Crack Defects," *Ceramic International*, **24**, pp 379-386.
- (5) Hadfield, M. and Stolarski, T.A. (1995), "The Effect of Test Machine on the Failure Mode in Lubricated Rolling Contact of Silicon Nitride," *Tribology International*, **28**, pp 377-382.
- (6) Rosado, L., Forster, N. and Thomson, K. (2008), "On the Rolling Contact Fatigue Life and Spall Propagation Characteristics of M50, M50 NiL and 52100 Bearing Materials: Part I: Experimental Results," presented at the STLE Annual Meeting, May 18-22, 2008, Cleveland, OH.
- (7) Forster, N.H., Ogden, W.P. and Trivedi, H.K. (2008), "On the Rolling Contact Fatigue Life and Spall Propagation Characteristics of M50, M50 NiL and 52100 Bearing Materials: Part III: Metallurgical Examination," presented at the STLE Annual Meeting, May 18-22, 2008, Cleveland, OH.

- (8) Hahn, G.T., Bhargava, V., and Chen, Q. (1990), "The Cyclic Stress-Strain Properties, Hysteresis Loop Shape, and Kinematic Hardening of Two High-Strength Bearing Steels," *Metallurgical Transactions A*, **21**, pp 653-665.
- (9) Vingsbo, O., and Osterlund, R. (1980), "Phase Changes in Fatigued Ball Bearings," *Metallurgical Transactions A*, **11A**, pp 701-707.
- (10) Voskamp, A.P. (1985), "Material Response to Rolling Contact Loading," *ASME J. Tribol.*, **107**, pp 359-366.
- (11) Voskamp, A.P. (1998), "Fatigue and Material Response in Rolling Contact," *Bearing Steels: Into the 20th Century*, **ASTM STP 1328**.
- (12) Voskamp, A.P., and Mittemeijer, E.J. (1997), "The Effect of the Changing Microstructure on the Fatigue Behavior During Cyclic Rolling Contact Loading," *Z. Metallkd.*, **88**, pp 310-319.
- (13) Voskamp, A.P. (2002), "Microstructural Stability and Bearing Performance," *Bearing Steel Technology*, **ASTM STP 1419**.
- (14) Voskamp, A.P., Nierlich, W., and Hengerer, F. (1997), "X-ray Diffraction Provides Answers to Bearing Failures," *SKF Evolution*, **4**, pp 25-31.
- (15) Voskamp, A.P., and Mittemeijer, E.J. (1997), "State of Residual Stress Induced by Cyclic Rolling Contact Loading," *Z. Materials Science and Technology*, **13**, pp 431-438.
- (16) Dommarco, R.C., Kozaczek, K.J., Bastias, P.C., Hahn, G.T., and Rubin, C.A. (2004), "Residual Stresses and Retained Austenite Evolution in SAE 52100 Steel under Non-Ideal Rolling Contact Loading," *Wear*, **257**, pp 1081-1088.
- (17) Turteltaub, S. and Suiker, A.S.J. (2005), "Transformation-Induced Plasticity in Ferrous Alloys," *Journal of Mechanics and Physics of Solids*, **53**, pp 1747-1788.
- (18) Voskamp, A.P. and Mittemeijer, E.J. (1996), "Crystallographic Preferred Orientation Induced by Cyclic Rolling Contact Loading," *Metallurgical and Material Transactions A*, **27A**, pp 3445-3465.
- (19) ABAQUS Reference and Theory Manual version 6.7, Dessault Systems 2007.
- (20) Zaretsky, E.V., Poplawski, J.V., and Peters, S.M. (1996) "Comparison of Life Theories for Rolling Element Bearings," *Tribology Transactions*, **39**, 2, pp 237-248.
- (21) Kotzalas, M. and Harris, T.A. (2001), "Fatigue Failure Progression in Ball Bearings," *Trans. ASME*, **123**, pp 238-242.
- (22) Xu, G. and Sadeghi, F. (1996), "Spall Initiation and Propagation Due to Debris Denting," *Wear*, **201**, pp 106-116.
- (23) Gupta, P.K. (1984), *Advanced Dynamics of Rolling Elements*, Springer-Verlag, New York.
- (24) Johnson, K.L. (1987), *Contact Mechanics*, Cambridge Press, Cambridge.
- (25) Rickerby, D.G. and McMillan, N.H. (1980), "On the Oblique Impact of a Rigid Sphere against a Rigid-Plastic Solid," *International Journal of Mechanical Sciences*, **22**, pp 491-494.
- (26) Hutchings, I.M., Rickerby, D.G. and McMillan, N.H. (1981), "Further Studies of the Oblique Impact of a Hard Sphere against a Ductile Solid," *International Journal of Mechanical Sciences*, **23**, pp 639-646.